



Article

Analyzing Changes in Urban Green Spaces and Their Effect on Land Temperature from the Perspective of Surface Radiation Energy Balance in Rizhao City, the Central Coast of China

Tao Pan ^{1,2}, Shanfeng He ^{1,*}, Zhaoyu Liu ³, Liming Jiang ¹, Qinglei Zhao ¹ and Rafiq Hamdi ^{4,5}

- ¹ Key Laboratory of Terrestrial Ecological Remediation in Jining City, School of Geography and Tourism, Qufu Normal University, Rizhao 276826, China; pantao@qfnu.edu.cn (T.P.); lyjiangliming@163.com (L.J.); qlzhao0119@qfnu.edu.cn (Q.Z.)
- ² Key Laboratory of Land Surface Pattern and Simulation, Institute of Geographic Sciences and Natural Resources Research, Chinese Academy of Sciences, Beijing 100101, China
- ³ School of Computer Science, Qufu Normal University, Rizhao 276826, China; zhylieu@qfnu.edu.cn
- ⁴ Royal Meteorological Institute, 1180 Brussels, Belgium; rafiq.hamdi@meteo.be
- ⁵ Department of Physics and Astronomy, Ghent University, 9000 Ghent, Belgium
- * Correspondence: hesf2020@qfnu.edu.cn; Tel.: +86-19862356365

Abstract: The greening of land plays a meaningful role in improving human settlements by regulating ecosystem functions in the central coast region of China. However, research on the spatiotemporal heterogeneity of green land changes in different urbanized regions and the cooling temperature effect of the different green land densities are still lacking in this region, which limits the understanding of the effect of greening of land on land thermal properties. To address this issue, we integrated several approaches to establish a comprehensive way of ‘human–computer interactive interpretation method—urban interior mixed pixel model—surface radiation energy balance model’ using data from remote sensing images and the national land use/cover database of China, focusing on Rizhao city. The conclusions are as follows: The total greening of land from 2000 to 2022 was monitored, and it was found that its cover improved within the built-up area of the city, with the proportion of green land increasing from 25.34% in 2000 to 42.98% in 2022. Differences in the amount of green spaces in different urbanized regions were first observed, namely, the urban greening rate was 37.78% in the old urban area in 2022, while it was as high as 46.43% in the newly expanded urban area in 2022, showing that more attention should be given to the construction of urban green spaces during urban expansion. Thermal comfort indicators in the study area were evaluated in terms of latent heat flux (0–457.83 W/m²), sensible heat flux (0–645.09 W/m²), and total available energy (254.07–659.42 W/m²). We also found that the cooling temperature effect in the middle- and high-density green land regions were 1.05 °C and 2.12 °C higher than those in the low-density region, and the established comfort/discomfort zones in terms of land surface temperature were depicted. These results provide a new practical reference for exploring the spatiotemporal heterogeneity change in green land and its impact on land-surface thermal properties in coastal regions.

Keywords: land use; urban green spaces; land surface thermal properties; central coast of China



Citation: Pan, T.; He, S.; Liu, Z.; Jiang, L.; Zhao, Q.; Hamdi, R. Analyzing Changes in Urban Green Spaces and Their Effect on Land Temperature from the Perspective of Surface Radiation Energy Balance in Rizhao City, the Central Coast of China. *Remote Sens.* **2023**, *15*, 4785. <https://doi.org/10.3390/rs15194785>

Academic Editor: Yuanjian Yang

Received: 22 August 2023

Revised: 24 September 2023

Accepted: 27 September 2023

Published: 30 September 2023



Copyright: © 2023 by the authors. Licensee MDPI, Basel, Switzerland. This article is an open access article distributed under the terms and conditions of the Creative Commons Attribution (CC BY) license (<https://creativecommons.org/licenses/by/4.0/>).

1. Introduction

Greening land has significant benefits in terms of reducing the land’s thermal properties and regulating ecosystem services. In hot summers, people are often attracted to the cooler climate of coastal cities [1]. However, in the context of rapid urbanization [2], reinforced concrete buildings may introduce the urban heat wave agglomeration effect and form a thermal discomfort region for residents in coastal urban areas [3–5]. A reasonable layout of urban green spaces can usually alleviate damage from extreme summer temperatures and avoid discomfort, such as heatstroke, for local residents or tourists,

thereby improving ecosystem services in this region [6,7]. Currently, China is still undergoing a rapid urbanization process, shifting from the old mode of unilateral pursuit of urban expansion to the new mode of rational urban land planning with a harmonious coexistence between people and natural environments [8,9]. In the context of the current urban construction of sponge cities, livable cities, innovative cities, and ecological cities in China, greening of land plays an increasingly important role in providing comfortable living environments and regulating ecosystem services [10]. Especially in the face of the aim of reaching a carbon peak in 2030 and carbon neutrality in 2060 in China, the city's carbon digestion capacity further requires the improvement of green land distribution patterns [11–13]. Studies monitoring the spatiotemporal heterogeneity changes in green spaces and analyzing their impact on residents' thermal comfort from the perspective of land-surface thermal properties have become hot topics.

Scholars have conducted extensive research on the spatiotemporal heterogeneity of the process of greening land and its change [14,15]. Early green land area surveys mainly relied on manpower and manual measuring equipment such as level gauges and theodolites. This type of measurement required many professionals, and the efficiency of the measurement was not high [16–18]. With the development of Earth remote sensing observation technology, satellite sensors can be used to obtain Earth's land surface types, such as green land cover [19–21]. The imaging resolution for monitoring land use and cover changes has increased from 1000 m to 300 m, 30 m, 10 m, or even sub-meter. In the context of current big data and cloud platforms, land cover monitoring has become more popular at the local, regional, and global scales [22]. In this process, many green land mapping products have emerged using remote sensing satellites, such as the global 30 m land mapping products from the National Bureau of Surveying and Mapping in China, the 10 m resolution global land cover mapping, 2017, from Tsinghua University, and the vector dataset of land use/cover changes across China from the Chinese Academy of Sciences [23]. Based on these green land data monitoring products, global land cover was becoming increasingly green (i.e., greening Earth) [24], which was especially prominent in China and India. China accounted for 25% of the global net increase in leaf area while accounting for only 6.6% of global vegetated area. The greening in China was mainly from forests (42%) and croplands (32%), but in India, the increased greening of land came mainly from croplands (82%), with a minor contribution from forests (4.4%) [24]. In urban areas, the cities were also becoming greener, especially in arid and semi-arid regions in Africa [25]. Meanwhile, among these typical land use products, the vector land product released by the Chinese Academy of Sciences has multiperiod data, including for 1980, 1995, 2000, 2005, 2008, 2010, 2013, 2015, 2018, and 2020, which can be used for a continuous analysis of the land status and its change trend. These data contained 25 land classification types, showing a very extensive land cover mapping ability. In many previous studies, these data achieved good land mapping and land change analysis results in all of China in both regional and local scale investigations [26–28]. Considering the relevance of multiple periods and the diversity of land classifications from the land use/cover data from the Chinese Academy of Sciences, these land data were applied in this study.

From the perspective of land surface thermal properties, land use/cover changes alter the surface thermal radiance, causing cooling or warming as well as energy effects, which can be used to assess the thermal comfort of residents. Previously, studies mainly focused on evaluating the effects of a building's thermal environment on workers [29]. Subsequently, the Universal Thermal Climate Index (UTCI) was proposed, in order to investigate the relationship between human settlements and factors of land surface convection, thermal radiation, and water evaporation [30,31]. Additionally, the impact of greening of land on the comfort of human settlements was continuously explored, considering the impact of vegetation's horizontal and vertical characteristics on the environment. Specifically, vegetation has a natural physical shielding property, which affects air flow and heat exchange through horizontal blocking effects, resulting in a decrease in ambient temperature, and vegetation further intercepts solar radiation through vertical shading, creating relatively

low-temperature areas under vegetation through shading [31,32]. Then, scholars conducted research on the comfort of the living environment from a perspective of greening land, using the temperature and humidity index, comfort index, and wind efficiency index in regions where urban spaces were being greened [33,34]. The popularization of remote sensing technology has led these studies to move from statistics to spatialized land mapping results, such as spatialized land-surface thermal property maps of land surface temperature, air temperature, net radiation, the Bowen ratio, latent heat flux, available flux, and sensible heat flux [35–38], and thus, this has become a popular research approach for investigating the impact of land use changes on surface thermal properties.

The central coastal region of China attracts tourists from all over the country due to the advantages of the natural environment such as a suitable climate and high levels of green vegetation. Currently, the investigation of changes following greening of land in this region is insufficient, which limits the understanding of the impact of green spaces on residents' comfort in this region. Rizhao city is located in the central coastal region of China. Since 2000, the urbanization process has been accelerating. In 2009, Rizhao won "the United Nations Habitat Award" for its outstanding achievements in "improving housing and infrastructure, and building a green home", and it was the only region in China to receive this honor that year. Subsequently, Rizhao entered a faster stage of urbanization and obtained more Chinese awards such as that of being a "greening city". Considering the suitable natural climate and high coverage of green land, Rizhao city is a typical area in terms of green land changes and its thermal property effects on the central coastal region of China.

Currently, the understanding of the spatiotemporal heterogeneity of land changes as a result of greening in the central coastal region of China is still insufficient. In particular, a comparison of green land changes at different urbanization levels and the cooling temperature effect of the different green land densities are lacking in this region, which restricts the exploration of the land surface thermal property effect of green land changes. Therefore, the aims of this study are to effectively monitor spatiotemporal changes in green land and analyze their impact on surface thermal properties. Specifically, the objectives are to (1) provide effective monitoring of the spatiotemporal heterogeneity of green land and capture its new spatiotemporal features from 2000 to 2022; (2) reveal the different levels of green land at different stages of urban development and provide the specific quantitative values; and (3) analyze the impact of green land density and its thermal protective effect on the residential environments and map the spatial distribution characteristics of uncomfortably cold and hot areas for urban residents. Finally, three aspects are discussed, namely, a very green and livable region on the central coast of China is discussed, the different green land changes in different regions of China and worldwide are compared, and the positive effects of dense greening of land on the comfort of urban residents are investigated.

2. Materials and Methods

2.1. Study Area

Rizhao is located in the mid-latitude region of the Earth's northern hemisphere, with a total area of 5330.72 km² in 2022, a longitude range of 118°25'~119°39'E, and a latitude range of 35°04'~36°04'N (Figure 1). Regarding the natural environment of the study area, the terrain exhibits a high numerical value in the middle and a flat surrounding area. This region has a temperate monsoon climate with a small temperature difference among the four seasons, meaning that the temperature in summer and winter is moderate, and the area holds abundant water resources. From the perspective of administrative division, a branch of socio-economic environments, Rizhao city contains over 30 administrative sub-regions.

Rizhao is an ecologically coastal, livable, tourism-based, modern port and the portside industrial base in China. It is also known as the "Capital of Water Sports" and "Oriental Sun City". Rizhao won the United Nations Habitat Award for its beautiful environment. Rizhao was also awarded the titles of National Civilized City, National Forest City, Na-

tional Environmental Protection Key City, and National Ecological Demonstration Zone Construction Pilot City. The pleasant ecology, livable environment, and high coverage of green land make Rizhao a suitable area for exploring the spatiotemporal features of green land changes and its effect on land thermal properties from the perspective of land surface radiation energy balance on the central coast of China.

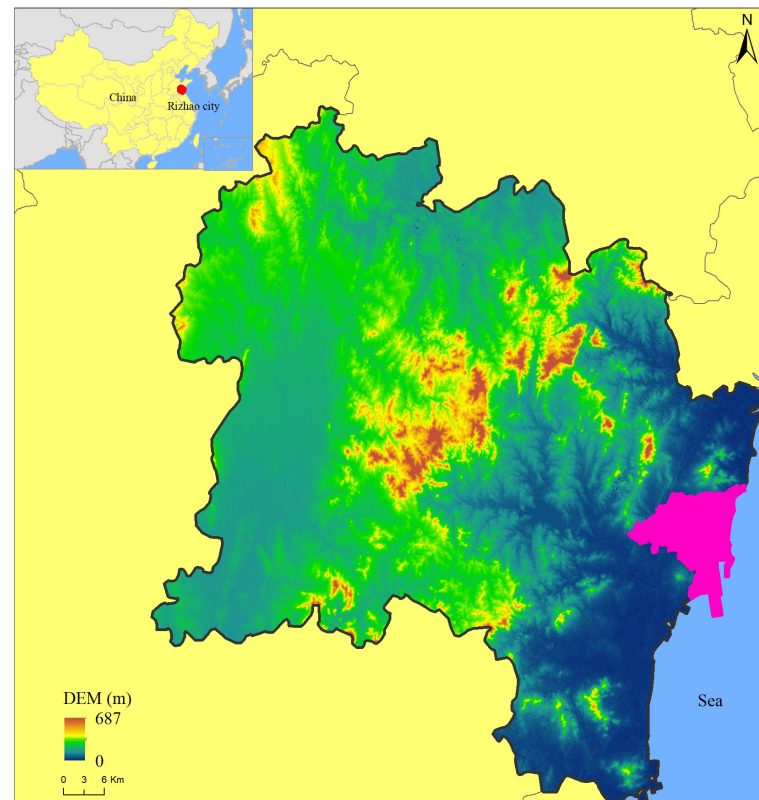


Figure 1. Geographical map of Rizhao City. Note: The upper left corner displays the location diagram, in which the red color indicates the location of Rizhao city in China. And in the enlarged picture, the pink color shows the location of the 2022 built-up area in Rizhao.

2.2. Data Collection and Preprocessing

2.2.1. Collection of Land Use Data

Land use data were very important for this study. Before the start of the study, we reviewed the datasets from Tsinghua University, from Wuhan University, from the Institute of Geographic Sciences and Natural Resources Research, Chinese Academy of Sciences, from the Institute of Remote Sensing and Digital Earth, Chinese Academy of Sciences, etc. All these data had good time series with high data consistency to use for studying land use and the monitoring of land use changes, but the data formats that were publicly available on the internet were grids [39–42]. Perhaps, the vector format of land use data was more convenient for calculation and statistics. As members of the land dataset group at the Institute of Geographic Sciences and Natural Resources Research, Chinese Academy of Sciences, we obtained the vector land dataset for the years of 2000 and 2015. To include the most recent land use change monitoring data, we extended the land use time to 2022. Then, the land data for the years of 2000 and 2022 were used in this study.

The land use/cover dataset from the Chinese Academy of Science was developed using the process of human–computer interactive interpretation of remotely sensed information to interpret the Landsat digital images covering China, and to construct the national land-use database [43,44]. For areas not covered by Landsat image data or covered with poor-quality data, supplemental data from the CCD multispectral data from the Huanjing-1 satellite (HJ-1) were used. The land changes were labeled with attribute codes using professional

geoscience knowledge, and the codes can simultaneously reflect the land use type of the dynamic plots during the different stages. The uniform quality control and integration checking for each dataset was used to ensure high-quality and consistent interpretation. The overall accuracies of datasets were above 91% [26,44] and meet the requirement of the user mapping. According to the land use classification system from the Chinese Academy of Sciences data, the first-level land types included 6 categories (i.e., cropland, forest land, grassland, water land, construction land, and unused land), and the second-level types included 25 categories. Rich land classification systems can monitor the land cover and its change more effectively [42,45].

2.2.2. Remote Sensing Image Download

The remote sensing images from 2022 were downloaded and preprocessed in this section (Section 2.2.2) and served as the basic data for producing land use maps for 2022. The United States Geological Survey (USGS) provided the free, universal, and better spectral characteristics of land resource satellites, and this was also the main data source for the land use data production process of the Chinese Academy of Sciences. To match the consistency between this image data source and the Chinese Academy of Sciences' land data, we used the remote sensing satellite from the USGS to obtain land use maps for 2022. For the satellite data quality inspection, Landsat OLI images with poor quality, bad pixels, and cloud cover were removed. This means that we focused on high-quality images covering the study area. For the time of image acquisition, we selected the summer of 2022, as the different types of land surface covers were relatively easy to identify in summer. Then, images with available observations and of high quality were downloaded for 2022, with the images' path and row number being 120,035. False color band synthesis was performed on these Landsat images. The data used in this study are displayed below (Table 1).

Table 1. The data used in this study.

Data Type	Data Name	Spatial Resolution/Format	Data Source/Links
Land use data	National land use/cover database of China in 2000 and 2015	vector	The Institute of Geographic Sciences and Natural Resources Research, Chinese Academy of Sciences
Remote Sensing data	Landsat Thematic Mapper (TM)	30-m	https://glovis.usgs.gov (accessed on 15 December 2022)
	Operational Land Imager (OLI)	30-m	https://glovis.usgs.gov (accessed on 15 December 2022)
	Digital Elevation Model (DEM)	30-m	https://glovis.usgs.gov (accessed on 15 December 2022)
	Google Images	0.5-m	http://www.91weitu.com (accessed on 15 December 2022)
Basic Geographic data	Administrative division	vector	https://www.resdc.cn (accessed on 15 December 2022)

2.3. The Technical Process of This Study

Main technical process of this study is shown in Figure 2. This technical process mainly included four steps. The objectives of steps 1 to 4 were to obtain the updated land use in 2022, the classified land covers within the built-up areas, and the calculated land surface temperature as well as the land surface thermal property indicators, and to perform the comprehensive analysis, respectively. Each step is explained in detail below.

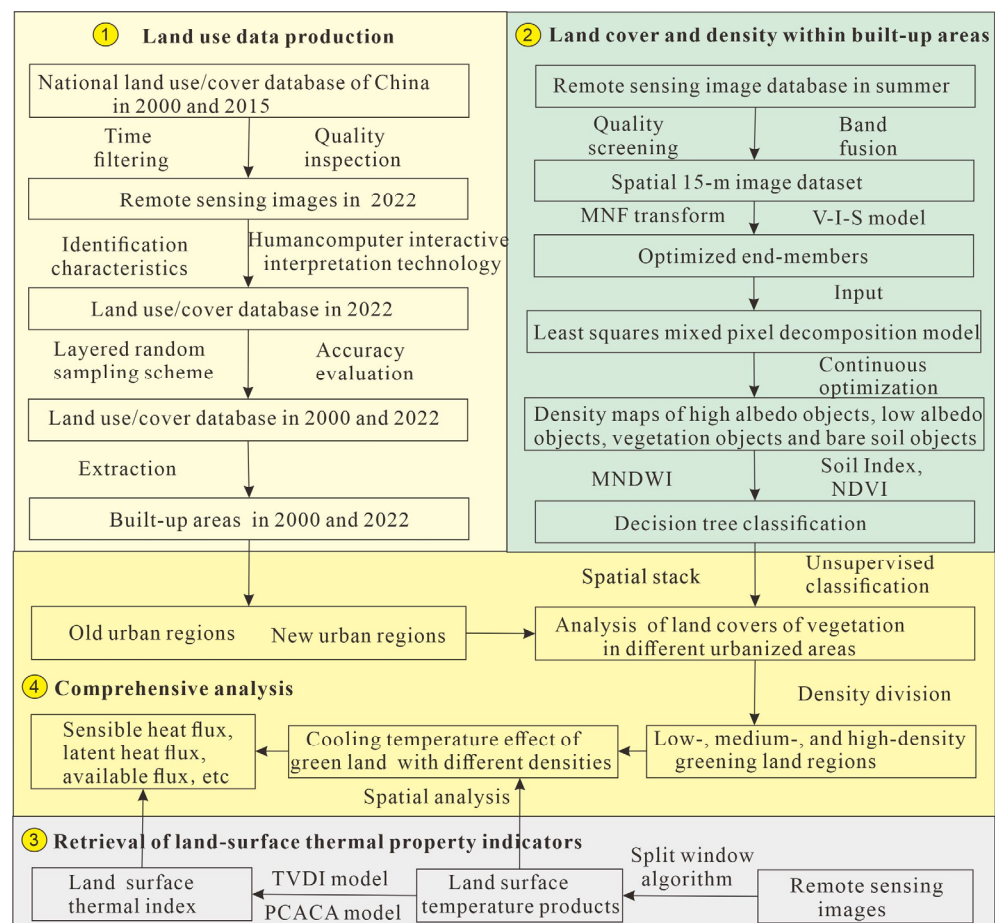


Figure 2. The technical flowchart of this study. Note: the arrows represent a sequence of data usage.

The first step was to obtain the latest land use mapping for the year of 2022, so that we could extract the built-up areas in the years of 2000 and 2022. We obtained land use data for the years of 2000 and 2015 from the Chinese Academy of Sciences. Based on the 2015 land use data, the traditional human–computer interactive interpretation process of remotely sensed information to interpret the Landsat digital images was applied in order to establish new land use maps for 2022 on the ArcGIS software platform. After producing the land use data, the accuracy evaluation was conducted using the method of layered random sampling through creating random points functions in the data management tools. Then, the land use data for the years of 2000 and 2022 were used to extract the built-up areas in the years of 2000 and 2022 for this study.

The second step was to obtain the greening of land within the built-up area, so that the spatiotemporal patterns of green land within the built-up area in different urbanization regions (i.e., the old and new urban regions) could be compared in order to delve deeper into the differences in land changes. For generating land cover within built-up areas, the vegetation–impervious surface area–soil model (V-I-S) from the ENVI software platform was used to obtain the optimal endmembers of the different types of land covers. In this model, the principal component transformation first concentrated the spectra of surface objects in the first three bands. A 2D scatter plot and band choice were used to combine the first three short waves in pairs. In these different combinations of windows, the land type features presented different scatter points. The land type spectrums of vegetation, impervious surface area, and soil can be obtained using the region of interest tool to select the corner points of these scatter points. These endmembers were input in the least squares mixed pixel decomposition model to generate the densities of high albedo objects, low albedo objects, vegetation objects, and bare soil objects. These four densities, as well as

other indexes, were used to generate the land cover of impervious surface areas, vegetation, bare soil, and water bodies, using the decision tree classifier method and unsupervised classification method. The vegetation cover was extracted using the select tool in the extract module on the ArcGIS platform. By using spatial overlay analysis tools, we superimposed urban built-up areas with vegetation data, and further analyzed the differences in area and proportion changes of vegetation between original and expanded urban built-up areas.

The third step was to obtain the land surface temperature retrieval and various thermal comfort indicators. The split window algorithm was used to generate the surface temperature pattern. The combination of the surface radiation energy balance model, the pixel component arranging and component algorithm model (PCACA), and temperature vegetation dryness index model (TVDI) was then used to obtain various thermal comfort indicators, such as the sensible heat flux, latent heat flux, and available flux on the ArcGIS and ENVI software platforms.

The fourth step was the comprehensive analysis to provide effective monitoring of the spatiotemporal heterogeneity of green land space and capture its new change characteristics from 2000 to 2022, reveal the different green land levels in different regions of urban development and provide their specific quantitative values, and to reveal the cooling temperature effect within different green land densities as well as the thermal comfort indicators.

2.4. Methodology of Digitizing the Land Use Map, Classifying the Green Land Density and Its Cover, and Retrieving the Land Surface Thermal Properties

2.4.1. Producing the New Land Use Map to Include the New Built-Up Area during 2000–2022

For generating the land use maps for 2022 in this study, we used the traditional process of human–computer interactive interpretation, which was the same method as was used for the data production process of 2000 and 2015 by the Institute of Geographic Sciences and Natural Resources Research, Chinese Academy of Sciences. Using the land use map of 2015 as the basic data source, the spatial land map of 2015 was superimposed onto the corresponding images from 2022 on the ArcGIS software platform. In the 2015 land use map, a 2022 attribute table field was added, which was used to obtain the land cover types in the year of 2022. Then, the human–computer interactive interpretation method of remotely sensed information was used to interpret the Landsat digital images using professional knowledge by identifying the color and texture of different land features on the Landsat images. The identified land type results were placed in the attribute table's 2022 field. After identifying the entire research area, a 2022 land spatial map was generated. To ensure the accuracy of the 2022 data, the land use dynamic patches during 2015–2022 were obtained through the calculation of the attribute table's 2015 and 2022 fields, and different remote sensing professionals conducted multiple reviews of these dynamic patches. Finally, a spatial land use map for 2022 was generated. Then, the different built-up areas in the years of 2000 and 2022 were extracted and calculated using the spatial statistics analysis tools on the ArcGIS software platform.

After producing the land use data for 2022, the layered random sampling scheme was used to achieve accurate evaluation with a total of 300 sampling points for 2022 (Figure 3) in the data management tools on the ArcGIS software platform. For the high-resolution Google satellite images, the data were not freely accessible in China. We obtained them on the paid and professional 91 bitmap platform. The images contained the following information: resolution: 0.5 m, date: from 1 July to 30 September 2016 and 2022, sensor: QuickBird, vendor: DigitalGlobe and Google. Then, the ground truth distribution samples, producer's accuracy, user's accuracy, total classified pixels, and other indicators of per land class were calculated in the accuracy evaluation matrix (Table 2). The overall obtained land use accuracy was 92.67% in 2022. This means that the land use data achieved good accuracy.

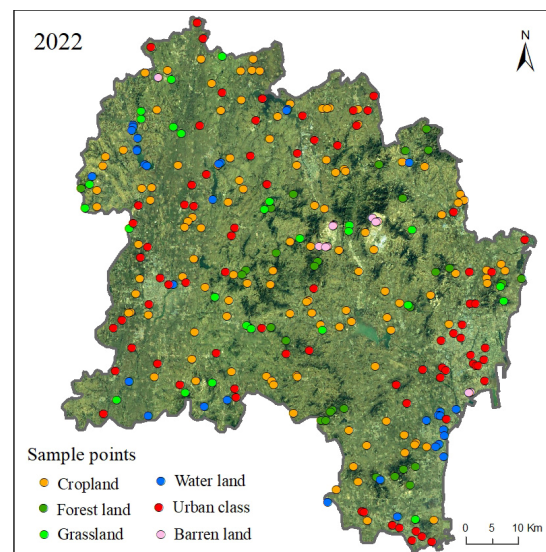


Figure 3. Spatial distribution of random land use sampling points for accuracy evaluation in 2022.

Table 2. Confusion matrix of land use validation according to Google images in 2022. The evaluated indicators such as overall accuracy (OA), user's accuracy, producer's accuracy, and kappa coefficients are also provided in this table [46].

Year	Land Use Type	Ground Truth (GT) Samples						Total Classified Pixels	User's Accuracy
		Crop Land	Forest Land	Grass Land	Water Land	Construction Land	Other Lands		
2022	Cropland	111	3	1	1	1	0	117	94.87%
	Forest land	2	27	1	0	0	0	30	90.00%
	Grassland	0	1	24	1	0	1	27	88.89%
	Water land	1	0	0	30	1	1	33	90.91%
	Construction land	2	1	1	0	73	1	78	93.59%
	Other lands	1	0	0	1	0	13	15	86.67%
	Total GT pixels	117	32	27	33	75	16	300	OA = 92.67%
	Producer's accuracy	94.87%	84.38%	88.89%	90.91%	97.33%	81.25%		Kappa = 0.88

2.4.2. Green Land Density Generation

Mapping of the density of green land can be used to comprehensively analyze the pattern change in the green land component and also to provide basic land data for investigating the cooling temperature effect from greening of land. To obtain different land type density maps (i.e., the area ratio of a land use type ranged from 0.01% to 100% within each grid pixel), the image band fusion technology was first used to upgrade the resolution of the satellite images from 30 m to 15 m [47] so that the land terrain pattern could be clearly depicted [48] on the ENVI software platform. After the band fusion, the minimum noise fraction rotation approach and the principal component analysis technology concentrated the spectral information on ground objects on the first three main bands. Through the V-I-S model, we obtained the endmembers in the land surface types of high and low albedo objects, greening land objects, and soil objects. Then, the endmembers were continuously optimized to obtain different land surface types of pure pixels, since the endmembers of pure pixels can obtain high-density maps of high and low albedo objects, greening land objects, and soil objects. In this process, we also used 0.5 m resolution Google satellite images to obtain different interpretation samples from some sample areas to assist in the density decomposition. After obtaining the endmembers of pure pixels, the least squares mixed pixel decomposition model was applied to obtain the density maps of different surface types (i.e., high and low albedo objects, greening land objects, and soil objects),

accompanied by corresponding density values of 0.01–100.00% at each grid pixel after the continuous end element optimization using the ENVI software platform.

In this study, the least squares mixed pixel decomposition model was applied, because it can effectively perform linear decomposition of different land use types with the advantage that the DN values of abundance maps for each end element within each pixel range from 0 to 1. The principle of the model is described as follows:

$$R_{i\lambda} = \sum_{k=1}^n f_{ki} C_{k\lambda} + \varepsilon_{i\lambda} \quad (1)$$

where $R_{i\lambda}$ is the albedo in the i -th pixel from band λ , f_{ki} is the proportion of the area occupied by k components in the i -th pixel, $C_{k\lambda}$ is the albedo in the k components from band λ , and $\varepsilon_{i\lambda}$ is the residual value.

2.4.3. Green Land Cover Classification

Green land classification was used to analyze the distribution of green land changes within the built-up area, further providing the differences in green land levels within different urbanization regions. To obtain green land classification data, we used a combination of supervised classification (i.e., decision tree) and unsupervised classification to elaborate the urban interior land classification map based on the different surface density data obtained in Section 2.4.2 using the ENVI software platform, thereby extracting the spatial distribution characteristics of green land. In the process, the improved normalized water body index was first input into the decision tree classification, with a threshold greater than 0 to obtain water coverage. Then, the high and low albedo object densities were used to generate impermeable surface areas and greening land density, normalized difference vegetative index (NDVI) was used to obtain vegetation coverage areas, and soil density was used to obtain soil coverage, resulting in the corresponding thresholds of 0.21, 0.18, 0.17, and 0.30 from impermeable surface areas, green land density, NDVI, and soil density, respectively. There were still some small areas that could not be classified by the remote sensing spectrum. Unsupervised classification divided these small mixed pixel distribution areas into 200 categories. Manual interpretation identified the land cover type that each classification belonged to. Then, the classification of green land within urban areas was composed of two-parts, including the decision tree results and the small patches of unsupervised classification results.

2.4.4. Calculation of Land-Surface Temperature

Considering the differences in the meteorological and environmental conditions during the different years of 2000 and 2022 and further avoiding systematic temperature errors, we used only remote sensing images from the summer of 2022 as an example to calculate the land surface temperature as well as to retrieve the land surface thermal property indicators. Land surface radiation energy is typically used to assess the effect of cold and heat on residents. For the surface energy distribution, the spatial distribution of the surface temperature should be presented first [36]. The split window algorithm model was used to produce spatiotemporal differences in temperature patterns, mainly based on the thermal infrared band of Landsat images and the related parameters in the python module on the ArcGIS platform. The main principles of the model are as follows [44]:

$$T_s = A_0 + A_1 T_{10} - A_2 T_{11} \quad (2)$$

$$A_2 = D_{10}/(D_{11}C_{10} - D_{10}C_{11}) + [D_{10}(1 - C_{11} - D_{11})/(D_{11}C_{10} - D_{10}C_{11})]/b_{11} \quad (3)$$

$$A_1 = 1 + D_{10}/(D_{11}C_{10} - D_{10}C_{11}) + [D_{11}(1 - C_{10}D_{10})/(D_{11}C_{10} - D_{10}C_{11})]b_{11} \quad (4)$$

$$A_0 = [D_{11}(1 - C_{10} - D_{10})/(D_{11}C_{10} - D_{10}C_{11})]\alpha_{10} - [D_{10}(1 - C_{11} - D_{11})/(D_{11}C_{10} - D_{10}C_{11})]\alpha_{11} \quad (5)$$

$$C_i = \varepsilon_i \tau_i(\theta) \quad (6)$$

$$D_i = [1 - \tau_i(\theta)][1 + (1 - \varepsilon_i)\tau_i(\theta)] \quad (7)$$

where, in Equation (2), T_s is the temperature of the land surface, T_{10} and T_{11} are the brightness temperatures obtained from Landsat images, and A_0 , A_1 , and A_2 are the transition parameters that can be calculated from Equations (3)–(7). For Equations (3)–(7), τ_i and ε_i represent the surface emissivity and atmospheric transmittance, which is also obtained from the calculation process of Landsat images.

2.4.5. Retrieval of Land Surface Thermal Property Indicators

On the basis of the calculated spatial surface temperature data, the surface radiation energy balance model was then used to obtain variously spatialized thermal comfort indicators, including the sensible heat flux, latent heat flux, and available flux. In this calculation process, some procedural parameters such as downwelling shortwave/longwave and upwelling longwave radiation were also calculated, using the parameter model to obtain the different flux data. The sensible heat flux was used to identify heat generation regions to explore its impact on residents, latent heat flux was used to explore suitable regions for residents' leisure activities, and available flux was used to evaluate the total energy that residents obtained on the ArcGIS and ENVI software platforms. The main principles of the model are as follows [45]:

$$a = 0.356 \times p_2 + 0.13 \times p_4 + 0.373 \times p_5 + 0.085 \times p_6 + 0.072 \times p_7 - 0.0018 \quad (8)$$

$$R_n = (1 - \alpha)R_{sd} + R_{ld} - R_{lu} \quad (9)$$

$$R_n = S + L + G_{soil} \quad (10)$$

$$L = LAFR(R_n - G_{soil}) \quad (11)$$

$$S = SAFR(R_n - G_{soil}) \quad (12)$$

$$LAFR = tvdi(T_s \&ndvi) \quad (13)$$

$$SAFR = 1 - tvdi(T_s \&ndvi) \quad (14)$$

$$G_{soil} = (T_s - 273.15) / \alpha(0.0038\alpha + 0.0074\alpha^2)(1 - 0.98NDVI^4)R_n \quad (15)$$

$$AF = S + L \quad (16)$$

where, in Equations (8) and (9), α is the land albedo from Landsat band2, band4, band5, band6, and band7; and R_{sd} , R_{ld} , and R_{lu} represent the indicators of shortwave radiation, downwelling longwave radiation and upwelling longwave radiation from the Landsat calculation parameters, respectively. In Equation (10), S , L , and G_{soil} are the sensible heat flux, latent heat flux, and soil heat flux. These indicators were obtained from Equations (11)–(15). For Equations (11)–(15), the temperature vegetation dryness index (TVDI) was used as a process parameter for calculating vegetation cover and land surface temperature based on optical and thermal infrared remote sensing channel data in Landsat images. The SAFR and LARF are the proportional parameters that are calculated from the pixel component arranging and component algorithm model (PCACA) using the land surface temperature from Landsat images and NDVI from the near-infrared band and infrared band. In Equation (16), AF is the available flux, which can be calculated using the sensible heat flux and latent heat flux.

3. Results

3.1. Analysis of Spatiotemporal Patterns of Green Land Cover within Different Urbanization Regions from 2000 to 2022

3.1.1. Different Green Land Cover Proportion Changes in Built-Up Areas in 2000 and 2022

The green land covered an area of 13.27 km² in the built-up area, with an urban greening rate of 25.34% in 2000 (Figure 4a). Regarding its spatial distribution, green land tended to be distributed intensively at the edge of the built-up area; in contrast, it was mainly distributed sporadically within the built-up area. Then, the coverage of the built-up area reached 130.89 km², with a total increment of 42.98 km² from 2000 to 2022. This result indicated that the increase in green land area was as high as 323.94% during the study period (Table 3). Therefore, by 2022, the urban greening rate of the study area reached 42.97% (Figure 4b), showing a very high proportion of green land coverage.

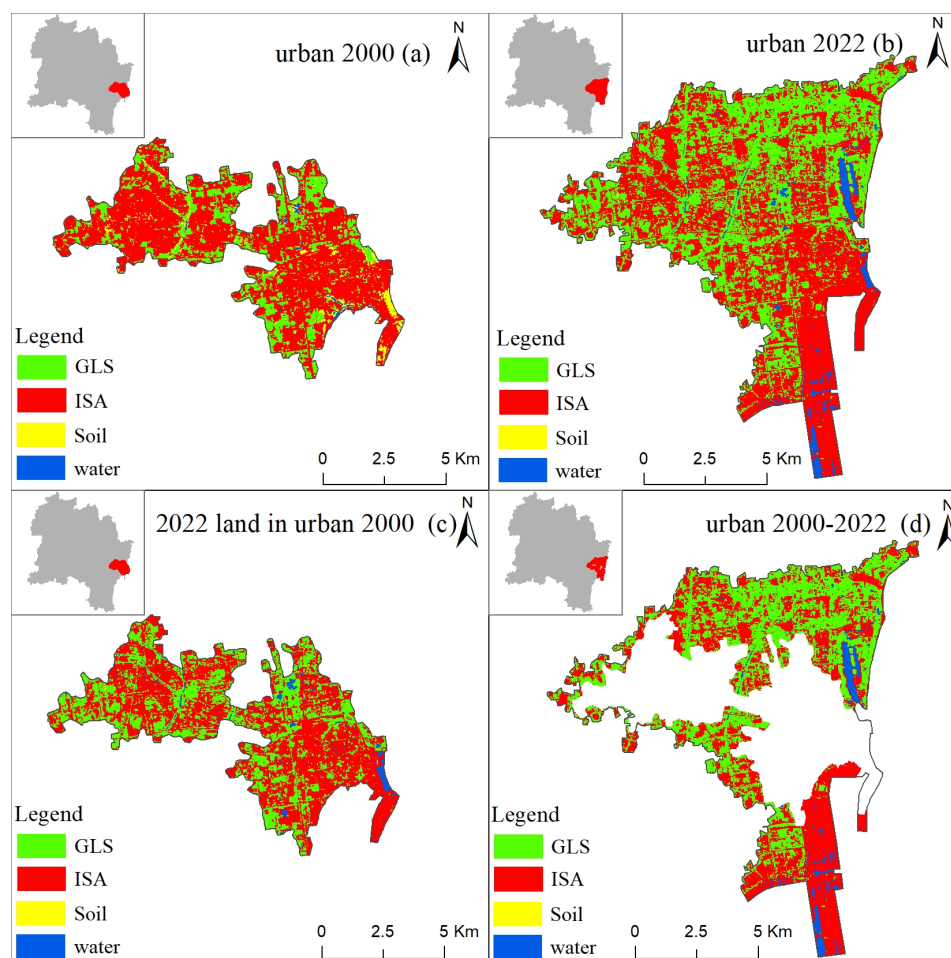


Figure 4. Spatial distributions of green land and non-green land cover within built-up areas. Notes: (a) 2000 land cover within built-up areas of 2000 and (b) 2022 land cover within built-up areas of 2022. The design of (a,b) was used to display the different land covers within the different built-up areas of 2000 and 2022, respectively. For (c), the 2022 land covers within the built-up areas of 2000 are shown, and (d) shows the 2022 land covers within the expansion region of built-up area during 2000–2022. The design of (c,d) was used to compare the different 2022 land covers within the boundary of the 2000 built-up area and the boundary of the expanded built-up area of 2000–2022, respectively. In the upper left corner of (a–d), we added the corresponding location figure of this region to the whole Rizhao city, in which the red regions represent the enlarged land covers within the built-up areas in (a–d), respectively. For the abbreviations in the legend of Figure 4, GLS: green land space, ISA: impermeable surface area.

Table 3. Statistics on the proportion of green land space in different urbanization regions.

Urbanization Regions	Area (km ²)	Proportion (%)
Green land cover in urban area 2000	13.27	25.34
Green land cover in urban area 2022	56.25	42.97
2022 green land cover in urban area 2000	19.78	37.78
Green land cover in urban area 2000–2022	36.47	46.43

3.1.2. Green Land Cover Levels in Different Urbanization Regions from 2000 to 2022

Here, the different green land levels in the old (Figure 4a) and new (Figure 4d) urbanization regions were compared. For the old urban region (i.e., the built-up area boundary in 2000 (Figure 4a,c)), which represents a fixed built-up area boundary scenario, the total area of green land was 19.78 km² in 2022 (Figure 4c), which was an increase of 6.51 km² compared with that in 2000 (i.e., 13.27 km² (Figure 4a)). With the boundary of the built-up area unchanged, the increase in green land space in the old urban regions means the improvement of green land service functions for residents, such as more places to rest in summer, more beautiful green landscapes, and more suitable green space temperature regulation.

Then, the green land levels in different built-up area scenarios (i.e., old and new built-up areas (Figure 4c,d) in a fixed year (i.e., 2022) were compared. Here, the newly built-up area was a region of urban expansion from 2000 to 2022 (Figure 4d). In 2022, the total area of green land in the newly built-up area was 36.47 km². Correspondingly, the greening rate of the newly built-up area reached 46.43%, accounting for nearly half of the proportion. Meanwhile, the greening rate of the old built-up area was 37.78% (Figure 4c). The data indicated that the rate of greening of land in the new urban area was 9.96% higher than that of the old urban area in 2022. Overall, we found that the order of greening level from high to low was new built-up area in 2022 (Figure 4d), old built-up area in 2022 (Figure 4c), and old built-up area in 2000 (Figure 4a).

3.2. Analyzing the Characteristics of Green Land Densities and Land Surface Thermal Comforts That Affect Residents

3.2.1. Analysis of the Characteristics of Green Land Density in Built-Up Areas

To further display the distribution of green land in urban areas, a green land density map was produced, with values in each grid pixel between 0.01% and 100%. The advantage of measuring green land density is that it can accurately depict the proportion of green land space per pixel. Figure 5 shows that the maximum green land density in the entire urban area can reach 100%. Through calculation, the average green land density in the entire area was shown to be 43.35%. For spatial patterns, the density of green land coverage was generally high on both sides of the roads and in concentrated park areas, where green land was widely planted, bringing comfort to residents. The low-value areas of green land density were concentrated mainly in the southeast region, which was the port, where the surface was mainly composed of roads, squares, and port construction facilities, and the green land design was relatively lower.

3.2.2. Analysis of the Spatial Distribution Characteristics of Thermal Comfort Factors Affecting Residents

From the perspective of residents' actual and perceived energy, the sensible heat flux, latent heat flux, and total available flux in built-up areas were selected to provide quantitative values and analyze the potential thermal comfort effect on residents. In particular, the sensible heat flux was used to understand the spatial pattern of heat generation. In contrast, latent heat flux primarily identified the areas of supercooling. The total available flux varied in different regions and at different latitudes, so this was also an important indicator used to characterize the total available energy that people obtained in a specific region.

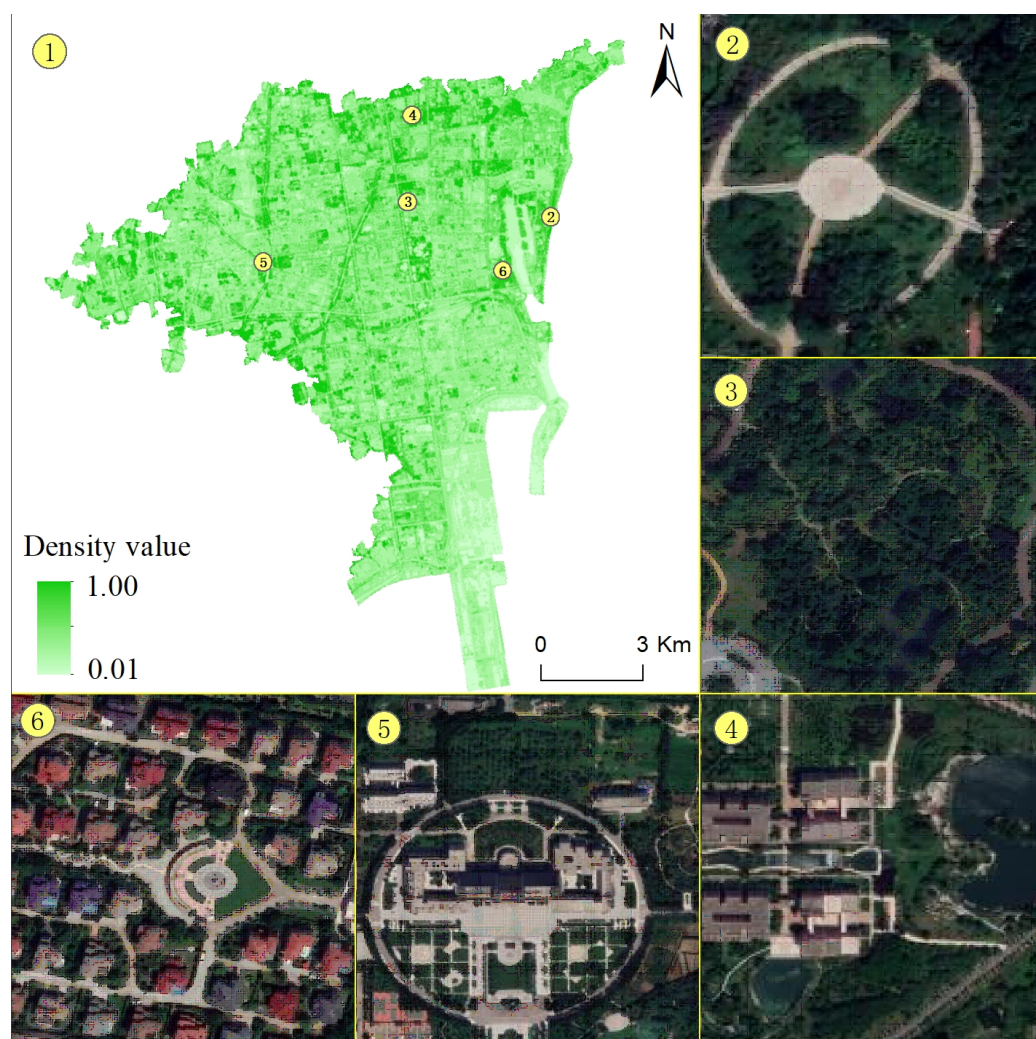


Figure 5. Spatial distribution of green land density. Notes: Labels 1, 2, 3, 4, 5, and 6 represent the regions of the green land density in the whole region, coastal green land, parks, recreational green spaces, office green spaces, and residential green spaces, respectively.

For sensible heat flux, the distribution map of sensible heat flux shows (Figure 6a) that the lowest value of the entire urban area was 0, indicating that some areas within the urban area did not display any sensible heat energy, and there was no heat source in these areas. The highest value was 457.83 W/m^2 , indicating that in local areas, the heat emission was still very high. We found that the sensible heat flux in urban areas presented a significant gradient feature, namely, the high value areas were concentrated mainly in the western region, which was also mainly the old urban area where the construction of houses, roads, and squares was relatively dense. In contrast, the low-value areas were distributed in the eastern region, which had a large distribution of green land.

For latent heat flux, the highest latent heat flux was 645.09 W/m^2 and was mainly distributed in the eastern part of the urban area (Figure 6b), close to the seaside, which was also the location of the Shanhaitian National Tourism Resort, indicating that this area generally had a higher latent heat flux than other areas, providing residents with a more cool and comfortable environmental feeling. Meanwhile, it was also seen that the highest values generally occurred in water bodies. Thus, concentrated and contiguous rivers, ponds, and fountains can provide a comfortable water environment for residents.

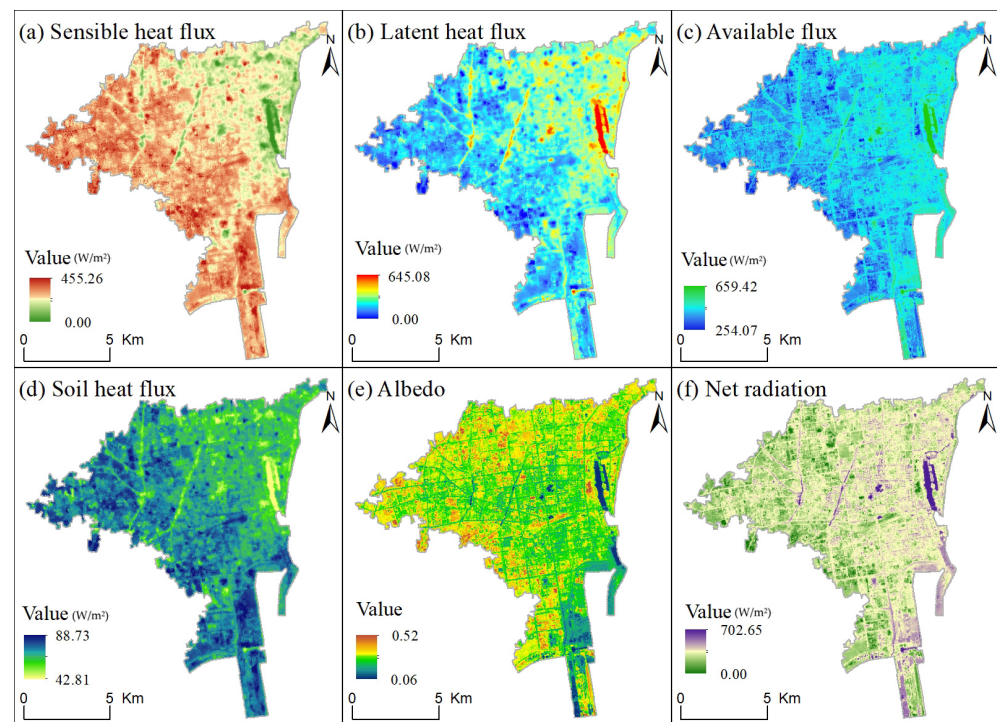


Figure 6. Spatial maps of sensible heat flux, latent heat flux, available flux, soil heat flux, albedo, and net radiation.

For total available flux, the lowest available flux was 254.07 W/m^2 (Figure 6c). We further determined that the maximum energy value was 659.42 W/m^2 , which was the maximum superposition of latent heat flux and sensible heat flux; thus, this value was higher than the maximum value of a single latent heat flux or a single sensible heat flux. The change in total available flux means a change in energy, which has impacts on residents' comfort perception. Through calculation, the average value of available flux was shown to be 492.75 W/m^2 . This is the first study to represent the average impact of the total energy available per unit area of the study area on the thermal comfort of residents. Then, spatial distribution maps of other thermal comfort factors such as soil heat flux, albedo, and net radiation were calculated and are displayed in Figure 6 to provide the specific quantification values of surface thermal properties.

3.3. Analysis of the Cooling Effect of Green Land and Its Impact on Urban Residential Environments

The cooling temperature effect of the density of green land was investigated using green land density data and land surface temperature data. The green land density data, with values ranging from 0.01% to 100% at each grid pixel, were divided into three levels, namely, low-, medium-, and high-density, with corresponding density values from 0.01% to 33.33%, 33.33% to 66.66%, and 66.66% to 100.00%, respectively. By superimposing these three density areas onto the land surface temperature, the cooling temperature values in the middle- and high-green-land-density regions were determined; the values were $1.05 \text{ }^\circ\text{C}$ and $2.12 \text{ }^\circ\text{C}$ higher than the corresponding low-density values. Therefore, the land temperature reduction effect of the green land became stronger as the green area coverage increased, even by over $2 \text{ }^\circ\text{C}$, compared with the low-green-land-density region on the central coast of China.

In addition to analyzing the cooling effect of green land areas, the discomfort from cold and heat experienced by residents and caused by land surface temperature was analyzed. The minimum land surface temperature in urban areas was $15.85 \text{ }^\circ\text{C}$ (Figure 7a) and this was distributed mainly in areas where rivers were concentrated. In contrast, the maximum land surface temperature was $36.64 \text{ }^\circ\text{C}$ and was mainly concentrated in the polymerization

effect area of buildings. Therefore, the variation range of the temperature was $18.79\text{ }^{\circ}\text{C}$ and the average temperature was $25.86\text{ }^{\circ}\text{C}$. According to relevant references, we set a temperature above $30\text{ }^{\circ}\text{C}$ as a thermal discomfort zone (Figure 7 upper left figure, red legend) and the temperature region below $18\text{ }^{\circ}\text{C}$ as a cold discomfort zone (Figure 7, upper right corner, blue legend). The spatial distribution of uncomfortable areas is displayed in Figure 7b,c. The proportions of hot and cold uncomfortable regions were 4.22% and 5.15% in the built-up area, respectively.

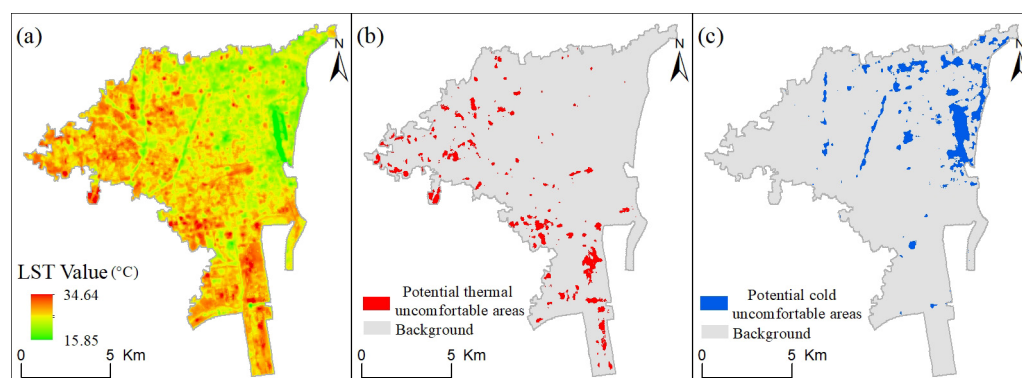


Figure 7. (a) Temperature distribution and corresponding comfort (b) and discomfort (c) regions from land surface temperature perspective. Abbreviation: LST: land surface temperature.

4. Discussion

4.1. A Highly Green and Livable Region on the Central Coast of China

To explore the spatiotemporal heterogeneity of green land change on the central coast of China, a typical region (i.e., Rizhao region) was investigated in this study. The first important finding was that the study area was a highly green region in China. We found a high coverage of green land areas, and evident differences in urban greening rates among different urbanization regions were revealed. In 2000, the greening rate was 25.34% in the built-up area, and it increased to 42.97% in 2022, with a percentage increment of 17.63%. This means that the proportion of green spaces in urban development has significantly increased. The green land coverage rate in the study area was amongst the highest in China [49]. Urban design has paid more attention to the role of green spaces [49,50], which are good for ecosystem service function for residents, for example, by reducing land thermal properties, absorbing carbon dioxide, and releasing oxygen [51,52].

A high green vegetation rate holds a significant application value. From the monitoring of this study, the urban greening rate reached 46.43% in the new urban area (i.e., the urban expansion area from 2000 to 2022). This means that nearly half of the new urban area was covered by green land/. According to our field investigation, in the newly built-up area, the green land space included centralized and scattered park green spaces, community green spaces, road shade areas, parking lot shaded areas, three-dimensional configuration of grassland landscapes, the green of squares, trellises and flower racks, green boundary regions, greening around sports grounds, and green roofs. A high coverage of green spaces also attracted tourists from other places. The rich and beautiful green space design not only provides local residents with a comfortable feeling, but also attracts large numbers of foreign tourists. Also, it is more advantageous for urban planning departments to carry out greener urban construction.

4.2. Comparison of the Differentiated Green Land Changes in Different Regions of China and Worldwide

Urban green spaces under different climatic backgrounds were first compared in China. In western China, especially in arid/semi-arid regions of northwest China [53–55], large-scale greening of areas was usually carried out in urban areas to provide better ecosystem services for residents. However, constrained by the arid climate, the proportion

of green land was always less than 20% in urban regions in northwest China. In contrast, in eastern China, a humid and semi-humid region [56–58], the proportion of green land areas within cities was relatively high, such as in Beijing, the capital city of China, where the proportion of green spaces was nearly 30% in built-up areas in the year of 2021. Further, in the coastal regions, the proportion of green spaces in built-up areas has further increased, such as in the study area of this paper, and the value rose to approximately 43% in the year of 2022. Under different climate backgrounds, the proportion of urban land that is green land resulted in huge differences.

Then, for different regions of the world, such as in Asia, green spaces in urban areas were then discussed. Relevant research indicated that the proportion of urban green land to the corresponding built-up area boundary decreased by 13.93% and 7.28% in capital cities of East Asia and South Asia from 2000 to 2015 [59]. By contrast, increases happened in the Middle East and Central Asia, with the incremental values of 12.61% and 15.36%, respectively. As for Europe, the spatial patterns of the cities were basically stable, with relatively small changes in green land. The increase in the proportion of green land was only 1.57%.

4.3. Possible Positive Effects of Densely Green Land Space on Human Welfare

Differences in green land coverage in different urbanized regions were observed, namely, the urban greening rate was 37.78% in the old urban area of 2022, while it was as high as 46.43% in the newly expanded urban area of 2022, showing that more attention should be given to the construction of urban green spaces during urban expansion. This finding shows that the creation of a high green coverage in newly expanded urban areas may have a positive impact on the living environment and residents' walking and travelling. First, it may increase aerobic exercise and improve the comfort of physical/mental health. Photosynthesis of forest and grassland in spaces with high rates of greening may promote the local production of a high-concentration "oxygen bar" environment [60], similar to a business place, but for people to breathe oxygen. When residents walk and rest in such a high-oxygen environment, their cerebral cortex and brain activities are strengthened, which may promote the absorption of oxygen, accelerate blood circulation, invigorate the spirit, eliminate fatigue, and improve immunity [61,62]. Second, it improves the comfort of leisure and improves mood [63,64]. According to our survey, the service radius required for Rizhao residents to reach parks and the centralized green space was less than 500 m. This was similar to the situation in areas of high greening in developed countries in the Americas and Europe, which featured a large population and high coverage of urban green spaces. Service radii shorter than 500 m from the park green space and the centralized green space were convenient for residents to stroll there and relax [65]. Most of their transportation methods for reaching these green regions are walking or cycling, which are not only green and environmentally friendly, but also have a mood-enhancing effect. However, if the service radius of park green spaces and centralized green spaces to people is large [66], such as in regions of Africa and other arid regions, people have to use private cars or public transportation to reach green land areas. This not only generates noise pollution and is prone to traffic congestion, which affects residents' moods, but also makes the exhaust gas from fuel-powered vehicles more likely to pollute the environment and generate greenhouse gas emissions, which is not conducive to the United Nations Sustainable Development Goals (i.e., SDGs [67]) target.

4.4. Limitations of This Study and Future Prospects

The impact of large-scale regional climate simulations on cities should be thoroughly investigated. This study focused on the central coastal areas of China, taking Rizhao City as an example, to monitor urban green land changes and analyze their effect on land thermal properties from a surface radiation energy balance perspective. Specifically, the spatiotemporal heterogeneity of green land changes in different urbanized regions was first revealed. The urban greening rate was 37.78% in the old urban area of 2022, while it was

as high as 46.43% in the newly expanded urban area of 2022, showing that more attention should be given to the construction of urban green spaces during urban expansion. Also, the cooling land surface temperature effect in the middle- and high-green-land-density regions was first studied, showing temperatures that were 1.05 °C and 2.12 °C higher than those in the low-density region. Thermal comfort indicators in the study area were also evaluated in terms of latent heat flux, sensible heat flux, and total available energy. All these results were regional investigations. As is known, Rizhao is a coastal city, and the sea should necessarily be taken into account at the regional climate scale. As a next step, we will elevate the investigation from the regional scale to large regional scale to comprehensively analyze the urban energy effect of green spaces and blue sea spaces using the Weather Research and Forecasting Model (i.e., WRF). Then, the comprehensive impact of green land and blue sea on the regional urban climate will be revealed.

More element indicators and green land types should be added. In the meanwhile, the cooling temperature effect of the density of green land was investigated using green land density data and land surface temperature data. The cold and hot discomfort zones of residents caused by land surface temperature were analyzed. In the next step of research, the proper comfort/discomfort zones based on more energy balance parameters should be investigated to conduct a more in-depth analysis from the comprehensive perspective of energy balance, such as by examining the factors of air temperature and relative humidity. The combination of the air temperature and the relative humidity can usually provide a comprehensive analysis of the impact of climate change on the comfort of urban living environments. Furthermore, in this study, urban green space was taken as a whole to explore the cooling effect of land surface on temperature. Although we obtained the cooling effect of green spaces at different densities (i.e., the low-, medium-, and high-density green land spaces), the different types of urban green such as shrubs, forested areas, and different types of grasslands may have different cooling effects on the land surface temperature. In future investigations, such a scientific issue will be summarized using the combination of high-resolution satellite images and surface radiation energy field observation.

More field observations on land surface temperature and its thermal properties should be investigated to conduct more in-depth research. Further, for the monitoring of green land areas, this study first analyzed the trend characteristics of green land changes throughout the whole Rizhao city using land use data. However, this land use classification system compiled the built-up area into one layer, which means that the monitoring of the green spaces within the built-up area cannot be carried out. The combination of V-I-S model—FCLS model—decision tree classifier—unsupervised classification was established to estimate green land cover and its density data using remote sensing images. Then, the green spaces pattern was monitored, and its cooling temperature effects were revealed within the built-up area. But the cooling temperature effects outside the built-up area were not investigated due to the relatively coarse 1 km resolution of the MODIS land surface temperature product and the inconsistency in the time of different Landsat images. The meteorological stations in the study were also relatively sparse. Therefore, more field observations on land surface temperature and its thermal properties should be conducted for more in-depth research, in order to reveal the cooling temperature effect of different green land types outside the built-up area in our study area. Finally, in this study, when we conducted land use accuracy assessments in 2022, high-resolution Google images were not free, which may have affected the universality of the data for other studies. In subsequent research, we will try our best to find free high-resolution remote sensing satellite data for land use accuracy evaluation.

5. Conclusions

This study investigated the spatiotemporal heterogeneity of green land changes in different urbanized regions and analyzed their effect on land thermal properties using the comprehensive method of human–computer interactive interpretation method—urban

interior mixed pixel model—surface radiation energy balance model to compensate for the lack of research on green land and its environmental effects on the central coast of China. For green land changes, remote sensing monitoring indicated that the green land proportion in old urban areas was 25.34% in 2000, and that this proportion increased to 37.78% in 2022. The increase in old urban areas means an improvement in the green land service function for residents. We also found that this proportion was as high as 46.43% in newly expanded urban areas, thus providing better visual and environmental comfort. The land thermal property indicators were also assessed, with values of 0–457.83 W/m² for latent heat flux, 0–645.09 W/m² for sensible heat flux, and 254.07–659.42 W/m² for total available energy in the study area. Furthermore, the cooling temperature effect from green land with different densities was revealed, with the lowered temperature values in the middle- and high-green-land-density regions being 1.05 °C and 2.12 °C higher than those of the low-density region. The minimum temperature was 15.85 °C and was distributed mainly in areas where rivers were concentrated. The maximum temperature was 36.64 °C and concentrated mainly in the polymerization effect area of buildings. Also, the spatial patterns of uncomfortably hot and cold areas were depicted. These results/findings provide a reference for the study of green land patterns and their impact on the land surface thermal properties of human settlements in coastal areas of China. This study also investigated the spatiotemporal heterogeneity of green land changes in different urbanized regions (i.e., the old and new urban regions) and the cooling temperature effect of the different green land densities in the central coast of China.

The contribution of this paper was to first compare the different greening levels in the old and newly expanded urban areas in the period of 2000–2022 and to provide the latest heterogeneity of green land changes on the central coast of China. The novelty was that the cooling land surface temperature effect of different green land densities (i.e., the low-, medium-, and high-density green space areas) was first revealed in the central coastal areas of China, and the relevant indicators of surface radiation energy balance were evaluated.

Author Contributions: Conceptualization, T.P. and S.H.; methodology, T.P.; writing—original draft preparation, T.P.; writing—review and editing, T.P., S.H., Z.L., L.J., Q.Z. and R.H. All authors have read and agreed to the published version of the manuscript.

Funding: This study is supported by the Natural science foundation youth program of Shandong Province (grant no. ZR2021QD134), Humanities and Social Sciences Foundation Project of Rizhao City in 2023 (grant no. 2023133), and the Young Taishan Scholars Program of Shandong Province (grant no. tsqn202103065).

Data Availability Statement: Not applicable.

Conflicts of Interest: The authors declare no conflict of interest.

References

1. Bell, S.L.; Phoenix, C.; Lovell, R.; Wheeler, B.W. Seeking everyday wellbeing: The coast as a therapeutic landscape. *Soc. Sci. Med.* **2015**, *142*, 56–67. [[CrossRef](#)]
2. Fu, S.; Zhang, X.; Kuang, W.; Guo, C. Characteristics of Changes in Urban Land Use and Efficiency Evaluation in the Qinghai–Tibet Plateau from 1990 to 2020. *Land* **2022**, *11*, 757. [[CrossRef](#)]
3. He, B.-J.; Wang, J.; Liu, H.; Ulpiani, G. Localized synergies between heat waves and urban heat islands: Implications on human thermal comfort and urban heat management. *Environ. Res.* **2021**, *193*, 110584. [[CrossRef](#)]
4. Zou, Z.; Yan, C.; Yu, L.; Jiang, X.; Ding, J.; Qin, L.; Wang, B.; Qiu, G. Impacts of land use/land cover types on interactions between urban heat island effects and heat waves. *Build. Environ.* **2021**, *204*, 108138. [[CrossRef](#)]
5. García, D.H. Analysis of urban heat island and heat waves using Sentinel-3 images: A study of Andalusian Cities in Spain. *Earth Syst. Environ.* **2022**, *6*, 199–219. [[CrossRef](#)]
6. Yin, J.; Fu, P.; Cheshmehzangi, A.; Li, Z.; Dong, J. Investigating the Changes in Urban Green-Space Patterns with Urban Land-Use Changes: A Case Study in Hangzhou, China. *Remote Sens.* **2022**, *14*, 5410. [[CrossRef](#)]
7. Wu, W.; Yuan, Y.; Huang, C.; Dong, W.; Fu, Z. Urban Green Land Ecological Suitability Assessment Based on GIS in Arid Areas: Beitun City, Xinjiang, as an Example. *Pol. J. Environ. Stud.* **2021**, *30*, 5871–5883. [[CrossRef](#)]
8. Liu, Y.; Zhou, Y. Reflections on China’s food security and land use policy under rapid urbanization. *Land Use Policy* **2021**, *109*, 105699. [[CrossRef](#)]

9. Tappert, S.; Klöti, T.; Drilling, M. Contested urban green spaces in the compact city: The (re-) negotiation of urban gardening in Swiss cities. *Landsc. Urban Plan.* **2018**, *170*, 69–78. [[CrossRef](#)]
10. Fan, F.; Lian, H.; Liu, X.; Wang, X. Can environmental regulation promote urban green innovation Efficiency? An empirical study based on Chinese cities. *J. Clean. Prod.* **2021**, *287*, 125060. [[CrossRef](#)]
11. Sun, L.-L.; Cui, H.-J.; Ge, Q.-S. Will China achieve its 2060 carbon neutral commitment from the provincial perspective? *Adv. Clim. Chang. Res.* **2022**, *13*, 169–178. [[CrossRef](#)]
12. Shi, X.; Zheng, Y.; Lei, Y.; Xue, W.; Yan, G.; Liu, X.; Cai, B.; Tong, D.; Wang, J. Air quality benefits of achieving carbon neutrality in China. *Sci. Total Environ.* **2021**, *795*, 148784. [[CrossRef](#)] [[PubMed](#)]
13. Wang, Y.; Guo, C.-H.; Chen, X.-J.; Jia, L.-Q.; Guo, X.-N.; Chen, R.-S.; Zhang, M.-S.; Chen, Z.-Y.; Wang, H.-D. Carbon peak and carbon neutrality in China: Goals, implementation path and prospects. *China Geol.* **2021**, *4*, 720–746. [[CrossRef](#)]
14. Guo, A.; Yang, J.; Sun, W.; Xiao, X.; Cecilia, J.X.; Jin, C.; Li, X. Impact of urban morphology and landscape characteristics on spatiotemporal heterogeneity of land surface temperature. *Sustain. Cities Soc.* **2020**, *63*, 102443. [[CrossRef](#)]
15. Yun, J.; Yu, W.; Wang, H. Exploring the Distribution of Gardens in Suzhou City in the Qianlong Period through a Space Syntax Approach. *Land* **2021**, *10*, 659. [[CrossRef](#)]
16. De Sousa, C.A. The greening of brownfields in American cities. *J. Environ. Plan. Manag.* **2004**, *47*, 579–600. [[CrossRef](#)]
17. Clark, M.L.; Aide, T.M.; Riner, G. Land change for all municipalities in Latin America and the Caribbean assessed from 250-m MODIS imagery (2001–2010). *Remote Sens. Environ.* **2012**, *126*, 84–103. [[CrossRef](#)]
18. Oleson, K.; Bonan, G.; Levis, S.; Vertenstein, M. Effects of land use change on North American climate: Impact of surface datasets and model biogeophysics. *Clim. Dyn.* **2004**, *23*, 117–132. [[CrossRef](#)]
19. Joyce, K.E.; Belliss, S.E.; Samsonov, S.V.; McNeill, S.J.; Glassey, P.J. A review of the status of satellite remote sensing and image processing techniques for mapping natural hazards and disasters. *Prog. Phys. Geogr.* **2009**, *33*, 183–207. [[CrossRef](#)]
20. Behnam, A.; Wickramasinghe, D.C.; Ghaffar, M.A.A.; Vu, T.T.; Tang, Y.H.; Isa, H.B.M. Automated progress monitoring system for linear infrastructure projects using satellite remote sensing. *Autom. Constr.* **2016**, *68*, 114–127. [[CrossRef](#)]
21. Treitz, P.; Rogan, J. Remote sensing for mapping and monitoring land-cover and land-use change—an introduction. *Prog. Plan.* **2004**, *61*, 269–279.
22. Amani, M.; Ghorbanian, A.; Ahmadi, S.A.; Kakooei, M.; Moghimi, A.; Mirmazloumi, S.M.; Moghaddam, S.H.A.; Mahdavi, S.; Ghahremanloo, M.; Parsian, S. Google earth engine cloud computing platform for remote sensing big data applications: A comprehensive review. *IEEE J. Sel. Top. Appl. Earth Obs. Remote Sens.* **2020**, *13*, 5326–5350.
23. Chen, B.; Xu, B.; Zhu, Z.; Yuan, C.; Suen, H.P.; Guo, J.; Xu, N.; Li, W.; Zhao, Y.; Yang, J. Stable classification with limited sample: Transferring a 30-m resolution sample set collected in 2015 to mapping 10-m resolution global land cover in 2017. *Sci. Bull.* **2019**, *64*, 370–373.
24. Chen, C.; Park, T.; Wang, X.; Piao, S.; Xu, B.; Chaturvedi, R.K.; Fuchs, R.; Brovkin, V.; Ciais, P.; Fensholt, R. China and India lead in greening of the world through land-use management. *Nat. Sustain.* **2019**, *2*, 122–129. [[CrossRef](#)]
25. Yin, Z.; Kuang, W.; Bao, Y.; Dou, Y.; Chi, W.; Ochege, F.U.; Pan, T. Evaluating the Dynamic Changes of Urban Land and Its Fractional Covers in Africa from 2000–2020 Using Time Series of Remotely Sensed Images on the Big Data Platform. *Remote Sens.* **2021**, *13*, 4288. [[CrossRef](#)]
26. Ning, J.; Liu, J.; Kuang, W.; Xu, X.; Zhang, S.; Yan, C.; Li, R.; Wu, S.; Hu, Y.; Du, G. Spatiotemporal patterns and characteristics of land-use change in China during 2010–2015. *J. Geogr. Sci.* **2018**, *28*, 547–562. [[CrossRef](#)]
27. Kuang, W.; Liu, J.; Dong, J.; Chi, W.; Zhang, C. The rapid and massive urban and industrial land expansions in China between 1990 and 2010: A CLUD-based analysis of their trajectories, patterns, and drivers. *Landsc. Urban Plan.* **2016**, *145*, 21–33.
28. Zhao, G.; Liu, J.; Kuang, W.; Ouyang, Z.; Xie, Z. Disturbance impacts of land use change on biodiversity conservation priority areas across China: 1990–2010. *J. Geogr. Sci.* **2015**, *25*, 515–529.
29. Nikolopoulou, M.; Baker, N.; Steemers, K. Thermal comfort in outdoor urban spaces: Understanding the human parameter. *Sol. Energy* **2001**, *70*, 227–235. [[CrossRef](#)]
30. Błażejczyk, K.; Jendritzky, G.; Bröde, P.; Fiala, D.; Havenith, G.; Epstein, Y.; Psikuta, A.; Kampmann, B. An introduction to the universal thermal climate index (UTCI). *Geogr. Pol.* **2013**, *86*, 5–10. [[CrossRef](#)]
31. Jendritzky, G.; Maarouf, A.; Fiala, D.; Staiger, H. An update on the development of a Universal Thermal Climate Index. In Proceedings of the 15th Conference Biometeorology and Aerobiology and 16th ICB02, Kansas City, MO, USA, 28 October–1 November 2002; pp. 129–133.
32. Yaghoobian, N.; Srebric, J. Influence of plant coverage on the total green roof energy balance and building energy consumption. *Energy Build.* **2015**, *103*, 1–13. [[CrossRef](#)]
33. Kuang, W.; Dou, Y. Investigating the patterns and dynamics of urban green space in China’s 70 major cities using satellite remote sensing. *Remote Sens.* **2020**, *12*, 1929. [[CrossRef](#)]
34. Young, R.F. Managing municipal green space for ecosystem services. *Urban For. Urban Green.* **2010**, *9*, 313–321. [[CrossRef](#)]
35. Lamchin, M.; Lee, J.-Y.; Lee, W.-K.; Lee, E.J.; Kim, M.; Lim, C.-H.; Choi, H.-A.; Kim, S.-R. Assessment of land cover change and desertification using remote sensing technology in a local region of Mongolia. *Adv. Space Res.* **2016**, *57*, 64–77. [[CrossRef](#)]
36. Yu, X.; Guo, X.; Wu, Z. Land surface temperature retrieval from Landsat 8 TIRS—Comparison between radiative transfer equation-based method, split window algorithm and single channel method. *Remote Sens.* **2014**, *6*, 9829–9852. [[CrossRef](#)]

37. Chakraborty, S.D.; Kant, Y.; Mitra, D. Assessment of land surface temperature and heat fluxes over Delhi using remote sensing data. *J. Environ. Manag.* **2015**, *148*, 143–152. [[CrossRef](#)] [[PubMed](#)]
38. Burakowski, E.; Tawfik, A.; Ouimette, A.; Lepine, L.; Novick, K.; Ollinger, S.; Zarzycki, C.; Bonan, G. The role of surface roughness, albedo, and Bowen ratio on ecosystem energy balance in the Eastern United States. *Agric. For. Meteorol.* **2018**, *249*, 367–376. [[CrossRef](#)]
39. Gong, P.; Wang, J.; Yu, L.; Zhao, Y.; Zhao, Y.; Liang, L.; Niu, Z.; Huang, X.; Fu, H.; Liu, S. Finer resolution observation and monitoring of global land cover: First mapping results with Landsat TM and ETM+ data. *Int. J. Remote Sens.* **2013**, *34*, 2607–2654. [[CrossRef](#)]
40. Gong, P.; Chen, B.; Li, X.; Liu, H.; Wang, J.; Bai, Y.; Chen, J.; Chen, X.; Fang, L.; Feng, S. Mapping essential urban land use categories in China (EULUC-China): Preliminary results for 2018. *Sci. Bull.* **2020**, *65*, 182–187. [[CrossRef](#)]
41. Yang, J.; Huang, X. The 30 m annual land cover dataset and its dynamics in China from 1990 to 2019. *Earth Syst. Sci. Data* **2021**, *13*, 3907–3925. [[CrossRef](#)]
42. Kuang, W.; Zhang, S.; Du, G.; Yan, C.; Wu, S.; Li, R.; Lu, D.; Pan, T.; Ning, J.; Guo, C. Monitoring periodically national land use changes and analyzing their spatiotemporal patterns in China during 2015–2020. *J. Geogr. Sci.* **2022**, *32*, 1705–1723. [[CrossRef](#)]
43. Liu, J.; Kuang, W.; Zhang, Z.; Xu, X.; Qin, Y.; Ning, J.; Zhou, W.; Zhang, S.; Li, R.; Yan, C. Spatiotemporal characteristics, patterns, and causes of land-use changes in China since the late 1980s. *J. Geogr. Sci.* **2014**, *24*, 195–210. [[CrossRef](#)]
44. Zhang, Z.; Wang, X.; Zhao, X.; Liu, B.; Yi, L.; Zuo, L.; Wen, Q.; Liu, F.; Xu, J.; Hu, S. A 2010 update of National Land Use/Cover Database of China at 1: 100,000 scale using medium spatial resolution satellite images. *Remote Sens. Environ.* **2014**, *149*, 142–154. [[CrossRef](#)]
45. Liu, J.; Liu, M.; Zhuang, D.; Zhang, Z.; Deng, X. Study on spatial pattern of land-use change in China during 1995–2000. *Sci. China Ser. D Earth Sci.* **2003**, *46*, 373–384.
46. Rwanga, S.S.; Ndambuki, J.M. Accuracy assessment of land use/land cover classification using remote sensing and GIS. *Int. J. Geosci.* **2017**, *8*, 611. [[CrossRef](#)]
47. Wyatt, C. *Radiometric Calibration: Theory and Methods*; Elsevier: Amsterdam, The Netherlands, 2012.
48. Cooley, T.; Anderson, G.P.; Felde, G.W.; Hoke, M.L.; Ratkowski, A.J.; Chetwynd, J.H.; Gardner, J.A.; Adler-Golden, S.M.; Matthew, M.W.; Berk, A. FLAASH, a MODTRAN4-based atmospheric correction algorithm, its application and validation. In Proceedings of the IEEE International Geoscience and Remote Sensing Symposium, Toronto, ON, Canada, 24–28 June 2002; pp. 1414–1418.
49. Piao, S.; Yin, G.; Tan, J.; Cheng, L.; Huang, M.; Li, Y.; Liu, R.; Mao, J.; Myneni, R.B.; Peng, S. Detection and attribution of vegetation greening trend in China over the last 30 years. *Glob. Chang. Biol.* **2015**, *21*, 1601–1609. [[CrossRef](#)]
50. Yao, L.; Li, T.; Xu, M.; Xu, Y. How the landscape features of urban green space impact seasonal land surface temperatures at a city-block-scale: An urban heat island study in Beijing, China. *Urban For. Urban Green.* **2020**, *52*, 126704. [[CrossRef](#)]
51. Shi, Y.; Shi, D.; Zhou, L.; Fang, R. Identification of ecosystem services supply and demand areas and simulation of ecosystem service flows in Shanghai. *Ecol. Indic.* **2020**, *115*, 106418. [[CrossRef](#)]
52. Wang, B.; Gao, P.; Niu, X.; Sun, J. Policy-driven China’s Grain to Green Program: Implications for ecosystem services. *Ecosyst. Serv.* **2017**, *27*, 38–47. [[CrossRef](#)]
53. Cao, S.; Chen, L.; Yu, X. Impact of China’s Grain for Green Project on the landscape of vulnerable arid and semi-arid agricultural regions: A case study in northern Shaanxi Province. *J. Appl. Ecol.* **2009**, *46*, 536–543. [[CrossRef](#)]
54. An, W.; Li, Z.; Wang, S.; Wu, X.; Lu, Y.; Liu, G.; Fu, B. Exploring the effects of the “Grain for Green” program on the differences in soil water in the semi-arid Loess Plateau of China. *Ecol. Eng.* **2017**, *107*, 144–151. [[CrossRef](#)]
55. Pan, T.; Lu, D.; Zhang, C.; Chen, X.; Shao, H.; Kuang, W.; Chi, W.; Liu, Z.; Du, G.; Cao, L. Urban land-cover dynamics in arid China based on high-resolution urban land mapping products. *Remote Sens.* **2017**, *9*, 730. [[CrossRef](#)]
56. Yu, L.; Liu, Y.; Liu, T.; Yan, F. Impact of recent vegetation greening on temperature and precipitation over China. *Agric. For. Meteorol.* **2020**, *295*, 108197. [[CrossRef](#)]
57. Li, Y.; Piao, S.; Chen, A.; Ciais, P.; Li, L.Z. Local and teleconnected temperature effects of afforestation and vegetation greening in China. *Natl. Sci. Rev.* **2020**, *7*, 897–912. [[CrossRef](#)] [[PubMed](#)]
58. Guo, R.; Bai, Y. Simulation of an urban-rural spatial structure on the basis of green infrastructure assessment: The case of Harbin, China. *Land* **2019**, *8*, 196. [[CrossRef](#)]
59. Pan, T.; Kuang, W.; Hamdi, R.; Zhang, C.; Zhang, S.; Li, Z.; Chen, X. City-level comparison of urban land-cover configurations from 2000–2015 across 65 countries within the Global Belt and Road. *Remote Sens.* **2019**, *11*, 1515. [[CrossRef](#)]
60. Boldina, A.; Chung, H.C.; Santos, A.M.C.; Steemers, K. Active urbanism: Heart rate and oxygen consumption comparison when walking on imitation steppingstones versus a plain surface. *Cities Health* **2022**, *7*, 398–415. [[CrossRef](#)]
61. Hall, C.; Knuth, M. An update of the literature supporting the well-being benefits of plants: A review of the emotional and mental health benefits of plants. *J. Environ. Hortic.* **2019**, *37*, 30–38. [[CrossRef](#)]
62. Park, S.; Kim, E.; Kim, G.; Kim, S.; Choi, Y.; Paek, D. What activities in forests are beneficial for human health? A systematic review. *Int. J. Environ. Res. Public Health* **2022**, *19*, 2692. [[CrossRef](#)]
63. Piva, G.; Caruso, L.; Gómez, A.C.; Calzolari, M.; Visintin, E.P.; Davoli, P.; Manfredini, F.; Storari, A.; Spinozzi, P.; Lamberti, N. Effects of forest walking on physical and mental health in elderly populations: A systematic review. *Rev. Environ. Health* **2022**. [[CrossRef](#)]
64. Peters, K. Being together in urban parks: Connecting public space, leisure, and diversity. *Leis. Sci.* **2010**, *32*, 418–433. [[CrossRef](#)]

65. Liu, H.; Li, F.; Li, J.; Zhang, Y. The relationships between urban parks, residents' physical activity, and mental health benefits: A case study from Beijing, China. *J. Environ. Manag.* **2017**, *190*, 223–230. [[CrossRef](#)] [[PubMed](#)]
66. Zhai, Y.; Wu, H.; Fan, H.; Wang, D. Using mobile signaling data to exam urban park service radius in Shanghai: Methods and limitations. *Comput. Environ. Urban Syst.* **2018**, *71*, 27–40. [[CrossRef](#)]
67. Fritz, S.; See, L.; Carlson, T.; Haklay, M.; Oliver, J.L.; Fraisl, D.; Mondardini, R.; Brocklehurst, M.; Shanley, L.A.; Schade, S. Citizen science and the United Nations sustainable development goals. *Nat. Sustain.* **2019**, *2*, 922–930. [[CrossRef](#)]

Disclaimer/Publisher's Note: The statements, opinions and data contained in all publications are solely those of the individual author(s) and contributor(s) and not of MDPI and/or the editor(s). MDPI and/or the editor(s) disclaim responsibility for any injury to people or property resulting from any ideas, methods, instructions or products referred to in the content.